Journal of Water Process Engineering 66 (2024) 106025

Contents lists available at ScienceDirect

Journal of Water Process Engineering

journal homepage: www.elsevier.com/locate/jwpe

# Polyacrylic acid functionalized superparamagnetic iron-oxide supraparticles for highly efficient adsorption and removal of contaminants from water

Mohaned Hammad [a,*,1], Adil Amin [a,1], Anam Asghar [b], Osama Anwar [a], Soma Salamon [c,f], Joachim Landers [c,f], Mena-Alexander Kräenbring [a], Adarsh Jain [a], Sebastian Hardt [e], Hartmut Wiggers [d,f], Torsten C. Schmidt [b], Heiko Wende [c,f], Christof Schulz [d,f], Doris Segets [a,f]

[a] *Institute for Energy and Materials Processes – Particle Science and Technology (EMPI–PST), University of Duisburg-Essen, Duisburg, Germany*
[b] *Instrumental Analytical Chemistry and Centre for Water and Environmental Research, University of Duisburg-Essen, Essen, Germany*
[c] *Faculty of Physics, University of Duisburg-Essen, Duisburg, Germany*
[d] *Institute for Energy and Materials Processes – Reactive Fluids (EMPI–RF), University of Duisburg-Essen, Duisburg, Germany*
[e] *HSWmaterials GmbH, Kamp-Lintfort, Germany*
[f] *Center for Nanointegration Duisburg-Essen (CENIDE), University of Duisburg-Essen, Duisburg, Germany*

## ARTICLE INFO

Editor: Ludovic F. Dumée

*Keywords:*
Superparamagnetic iron oxide
Spray-flame synthesis
Spray drying
Magnetic separation
Heavy metal ion adsorption

## ABSTRACT

Intensive research efforts have been devoted to remove trace amounts of toxic pollutants such as Ni(II) and Co(II) from water with the intention to provide clean fresh water to households. Iron-based adsorbents have attracted attention in the field of water purification because of their low cost, non-toxicity, and high availability in nature. However, due to their small volume, the recovery of the superparamagnetic iron-based adsorbents after the removal process in acceptably short times remains an unresolved research question. In this paper, we describe the fabrication of environmentally-friendly and superparamagnetic iron-oxide supraparticles optimized for the adsorption and removal of heavy metal ions and dyes from water with high recovery (within 20 s). The super-adsorbent iron-oxide supraparticles exhibited excellent removal efficiencies for Pb(II), Cr(III), Cd(II), Cu(II), Ni (II), Co(II), Li(I), and methylene blue (MB) with maximum adsorption capacities of 500, 446, 417, 366, 315, 294, 286, and 670 mg/g, respectively. Interestingly, the iron-oxide supraparticles with multicore structure revealed a higher saturation magnetization (72 $Am^2/kg$) when compared to the as-synthesized iron-oxide nanoparticles (61 $Am^2/kg$) that were used as starting material, facilitating fast recovery. The outstanding adsorption performance combined with the superparamagnetic properties and the high recovery demonstrates that low-cost iron-oxide supraparticles adsorbents can potentially be employed in water treatment and bioseparation.

## 1. Introduction

Water pollution caused by a wide variety of organic and inorganic compounds including toxic heavy metal ions has become a major concern that threatens healthy natural ecosystems due to industrial development and urbanization [1]. The failed attempt to treat waste containing persistent organic pollutants and heavy metal ions claims the lives of ~14,000 people on a daily basis [2]. In this regard, many heavy metals pose a widespread threat to aquatic organisms because of their high persistence, severe toxicity, bioaccumulation, and low degradability [3]. Heavy metals such as cadmium, lead, copper, and nickel can bind to proteins and nucleic acids within the human body, disrupting their cellular functions. This disruption may cause gradually progressing physical, muscular, and neurological degenerative processes that can imitate a number of severe illnesses, with repeated heavy metal exposure potentially causing cancer [4]. Hence, increasing effort is being devoted to explore treatment processes for the removal of heavy metals from various water bodies, including photocatalysis [5], membrane

---

[*] Corresponding author at: Institute for Energy and Materials Processes – Particle Science and Technology, University of Duisburg-Essen, Carl-Benz-Str. 199, 47057 Duisburg, Germany.

*E-mail address:* mohaned.hammad@uni-due.de (M. Hammad).

[1] These authors contributed equally to this paper.

https://doi.org/10.1016/j.jwpe.2024.106025
Received 28 April 2024; Received in revised form 30 July 2024; Accepted 18 August 2024

separation [6], chemical precipitation [7], ion exchange [8], electrolysis deposition [9], and adsorption [10]. Among these methods, adsorption is considered one of the most promising for removing heavy metals from water bodies due to its exceptional benefits, such as simple operation, low cost, high efficiency, reusability, and the wide availability of adsorbents [11].

Recently, iron-oxide nanoparticles (IONPs) have received attention in the field of water purification due to their low cost, easy surface modification, good biocompatibility, and chemical availability in combination with superparamagnetic properties [5]. The latter are of great importance for the recovery process while preventing premature particle agglomeration [12]. Nonetheless, due to their small volume, the recovery of the superparamagnetic IONPs after the adsorption process in a magnetic field in acceptably short time periods remains challenging, as the magnetic forces applied to each individual particle are small. Simply using larger iron-oxide particles is prohibitive as i) IONPs larger than ca. 50 nm are magnetically blocked in terms of superparamagnetic relaxation, thereby exhibiting strong magnetic interparticle interaction, and ii) because of the significantly reduced surface-to-volume ratio and thus lower specific surface area for adsorption.

Consequently, numerous studies aim at improving the magnetic separation as well as the adsorption capacity, e.g., by immobilization of IONPs on carbonaceous materials [13] or incorporating IONPs into polymers [14,15]. In these cases, the recovery of iron-oxide particles was enhanced by assembling multiple nanoparticles into larger multi-core particles. For instance, some reports have focused on synthesizing layered double hydroxide ion exchangers on superparamagnetic $SiO_2@Fe_3O_4$ microparticles for the removal of phosphate from wastewater [16]. These composite particles demonstrated high and selective uptake of phosphate after 24 h. Furthermore, a previous report showed that a hierarchical structure of carbon-coated iron microspheres as electrocatalytic denitrification exhibited excellent nitrate removal capacity after 24 h [17]. However, the utilization of complex carbonaceous structures and polymer host matrices poses challenges, particularly in terms of large-scale production and the methods used to load iron-oxide nanoparticles onto them, which may hinder their immediate applicability in industrial settings. Moreover, employing large carbonaceous structures may reduce the active iron-oxide content, necessitating a larger mass of adsorbent material to remove a certain concentration of pollutants.

Some authors documented the application of spray-dried hierarchical aggregates of iron-oxide nanoparticles in biotechnology for purifying recombinant proteins. They enhanced these aggregates by incorporating silica nanoparticles, resulting in a reduction of the initial magnetization from 45 to 15 A $m^2$/kg at 2 T [18]. Furthermore, other researchers have observed that coating the surface of iron-oxide nanoparticles with various surfactants and polymers decreases the overall magnetic phase, a critical parameter in numerous applications [19]. However, the use of spray-dried iron-oxide agglomerates (containing polyacrylic acid as additive) consisting of only IONPs without using additional host structures and matrices for the removal of heavy metal ions from water is not yet reported. As these agglomerates represent well-defined entities on the micrometer scale that are produced from defined colloidal nanoparticles as starting material [20], we and other researchers [21] call them supraparticles. To the best of our knowledge, this is the first study reporting the potential of magnetically enhanced iron-oxide supraparticles (IOSPs) for fast removal of highly concentrated heavy metals from water bodies within 60 min, demonstrating the high potential of poly (acrylic acid) functionalized supraparticles.

In this study, we present the scalable and reproducible synthesis of superparamagnetic IOSPs optimized for the adsorption and removal of heavy metal ions and dyes from water. The IONPs were synthesized using a spray-flame method [22], followed by spray drying of aqueous suspensions, which led to the formation of mechanically stable IOSPs. The primary objectives of this research are to develop IOSPs that are stable and porous while retaining or enhancing their superparamagnetic properties at the nanoscale, and to investigate their physicochemical and magnetic properties. We aim to assess the adsorption capacities of IOSPs for removing heavy metals such as Pb(II), Cr(III), Cd(II), Cu(II), Ni (II), and Co(II), which are commonly found in various water bodies. Additionally, we extend our investigation to the removal of lithium (Li), due to its increasing environmental presence and potential impact. Furthermore, we explore the adsorption capacity of IOSPs for a cationic dye, such as methylene blue (MB), addressing concerns about water pollution from diverse sources. Another key target is to evaluate the reusability of IOSPs in terms of their ability to uptake heavy metals over multiple cycles. Finally, we investigate the structural changes in IOSPs after the adsorption process and propose a mechanism for adsorption. These objectives aim to demonstrate the potential of IOSPs in water purification, providing a comprehensive understanding of their capabilities and limitations.

## 2. Material and methods

### 2.1. Materials

Poly(acrylic acid) (PAA, $(C_3H_4O_2)_n$, 240 kDa, 25 % (w/w) in water) and iron(III)-nitrate nonahydrate ($Fe(NO_3)_3$, ≥98 %) were received from VWR chemical. Solvents employed for nanoparticle synthesis acetic acid anhydride ($C_4H_6O_3$, ≥99 %), absolute ethanol ($C_2H_6O$), (2-ethylhexanoic acid ($C_8H_{16}O_2$, 99 %), and lead(II) nitrate ($Pb(NO_3)_2$, ≥99 %), cadmium(II) nitrate ($Cd(NO_3)_2$, ≥99 %), copper(II) nitrate ($Cu(NO_3)_2$, ≥99.9 %), cobalt(II) nitrate ($Co(NO_3)_2$, ≥98 %), nickel(II) nitrate ($Ni(NO_3)_2$, ≥99.99 %), chromium(III) nitrate ($Cr(NO_3)_2$, ≥99 %), and lithium(I) nitrate ($LiNO_3$, ≥99.99 %), and methylene blue ($C_{16}H_{18}ClN_3S$) for the adsorption tests were purchased from Sigma Aldrich. The source water contains natural organic matter (NOM), a diverse mixture of carbon-based compounds resulting from the decomposition of plant and animal matter. The Upper Mississippi River NOM (UMNOM, 1R110N) was obtained as dry solid extract from the International Humic Substances Society (IHSS, Saint Paul, MN, USA). UMNOM stock solutions were prepared by mixing 0.025 g of NOM in 50 ml of distilled water containing 0.1 M NaOH. The solution was shaken overnight, filtered through a polypropylene syringe filter with a pore size of 0.22 μm and adjusted to a pH value of 7 using $H_3PO_4$ (working solution). Double distilled water was used for the preparation of the stock solutions and the reaction solutions.

### 2.2. Preparation of mechanically stable IOSPs by non-reactive spray drying

IOSPs are susceptible to disassemble into individual nanoparticles after spray drying. PAA exhibits several advantages in this context, such as mechanical stability and electrostatic stabilization [21]. Therefore, two different batches (with and without PAA) have been prepared and investigated.

IONPs (1 g) were prepared according to the method detailed in our previous work [22] and summarized in the supplementary material, section 1.1. For generating a first batch of IOSPs (with PAA), IONPs were dispersed in 300 ml of water and sonicated for 15 min. The pH of the suspension was adjusted to 9 by adding 0.1 mol/l NaOH. Subsequently, pre-made dispersions of PAA (10 wt% in water) were added to the IONPs dispersion under sonication and the obtained mixtures were further stirred for another 30 min. Then, the dispersion was injected into a laboratory scale spray dryer (BÜCHI Labortechnik GmbH) with a feed rate of 5 ml/min using nitrogen as dispersion gas. A drying gas flow of 35 $m^3$/h nitrogen was used to prevent the oxidation of iron-oxide during the spray drying process. The drying temperature was set to 150 °C. The supraparticles were collected with a mass yield of 75 % (25 % were either too small/not agglomerated or too large) from the filter.

For the generation of a second batch, in order to investigate the effects of PAA on the particle properties, iron-oxide agglomerates (IOAgs) were prepared by the same spray drying settings, however, without introduction of PAA in the feed dispersion. These IOAgs served as a reference for IOSPs throughout the whole study.

## 2.3. Characterization methods

### 2.3.1. Structural characterization

X-ray diffraction (XRD, Cu Kα radiation, 2θ range: 10–80°) was used to verify the iron-oxide structure and to probe structural changes in IOSPs. The material composition was analyzed pre and post adsorption via X-ray photoelectron spectroscopy (XPS). Additional characterizations including transmission electron microscopy (TEM), scanning electron microscopy (SEM), $N_2$ physisorption (Brunauer–Emmett–-Teller), thermogravimetric analysis (TGA), zeta ($\zeta$) sizer analysis, sedimentation profiles, Fourier transform infrared spectra (ATR-FTIR), magnetometry and Mössbauer spectroscopy analysis (Mössbauer spectroscopy), and mercury intrusion porosimetry (MIP) were conducted. Details on sample preparation and measurement settings are summarized in the supplementary material, section 1.2.

### 2.3.2. Adsorption studies and analyses

The adsorption capacities were evaluated using a beaker flask (50 ml) filled with 10 mg of adsorbent sample added to a 20 ml metal ion solution (50 mg/l) and shaken at a speed of 200 rpm at room temperature. To adjust the pH to the required value, 0.1 mol/l HCl or 0.1 mol/l NaOH solution was used. To analyze the residual metal ion concentration, 1 ml of the suspension sample was taken out at different contact times and the adsorbent material was removed by an external magnet. The supernatant was evaluated for residual metal ion concentration using an atomic absorption flame emission spectrophotometer (AA-6200, Shimadzu). The same procedure was repeated with MB, and the MB residual concentration was quantified at a wavelength of 664 nm by UV–Vis spectroscopy (Varian Cary 400). From this data, the adsorption capacity $q_e$ (mg/g) of the adsorbent was calculated according to:

$$q_e = \frac{(C_0 - C_e)\ V}{m} \tag{1}$$

where $C_0$ (mg/l) is the initial concentration and $C_e$ (mg/l) is the equilibrium concentration of pollutant in the continuous phase, $V$ (l) the volume of the initial pollutant solution, and $m$ (g) the weight of the adsorbent material.

The adsorption isotherms were studied at different initial concentrations of metal solution (25–500 mg/l) at 298 K. Moreover, to study the reusability and stability of the adsorbent, the spent supraparticles were added to 0.1 mol/l HCl for 200 min, then washed two times with 0.1 mol/l HCl and three times with de-ionized water and then re-dispersed into a fresh metal solution for the next cycle. The adsorption percentage was calculated according to:

$$\text{Removal}\ (\%) = \frac{(C_0 - C_e)}{C_0} \times 100 \tag{2}$$

## 3. Results and discussion

### 3.1. Structural characterization of powders

The structure and crystallinity of the annealed IONPs, IOAgs, and IOSPs were characterized by XRD measurements and are shown in Fig. 1a. The (111), (220), (311), (400), (422), (511), (440), (620), and (533) diffraction peaks of all samples match the Bragg reflections of the spinel ferrite structure (ICSD card 98-015-8745). Since magnetite and maghemite have a similar crystal structure, the presence of magnetite and/or maghemite cannot be reliably distinguished from XRD patterns alone. However, it is important to note that the reflexes are broadened for small NPs, thus making it difficult to clearly distinguish between or quantify these two phases. Despite this, the lattice constant calculated from Rietveld refinement for all samples was determined to be 0.839 nm, suggesting the predominant formation of the magnetite phase [23]. The average crystallite size determined by Rietveld refinement of the XRD pattern for IONPs, IOAgs, and IOSPs are 7.4, 11, and 7.6 nm, respectively (supplementary material, Fig. S1). Despite the aggregation observed in IOAgs, an unexpected improvement in crystallinity was observed compared to the individual nanoparticles in IONPs and IOSPs. This increase in crystallinity may be attributed to aggregation-induced phenomena such as Ostwald ripening or the formation of larger, more uniform structures during spray drying. Ostwald ripening is a phenomenon where smaller nanoparticles dissolve and subsequently redeposit onto larger ones. This process selectively promotes the growth of larger, more crystalline particles while reducing the presence of smaller, less crystalline particles. In contrast, there was no obvious change in the crystallite size in the case of IOSPs where PAA was added to the spray drying mixture. The specific interaction between PAA and IONPs before the spray drying process could also be confirmed by the results from the FTIR measurements. Details are given in the supplementary material, Fig. S2.

To further understand the structural change of the iron-oxide material obtained after spray drying, Raman spectroscopy was employed to identify the oxidic nature of the iron-oxide materials and to distinguish between magnetite ($Fe_3O_4$) and maghemite ($\gamma$-$Fe_2O_3$) (Fig. 1b). The peak of all samples around 660 $cm^{-1}$ can be ascribed to the magnetite phase [24]. In good agreement with XRD data, there is no structural transformation of the magnetite phase after spray drying. However, it is important to mention that over time, such as after a few weeks of storage at ambient air, Mössbauer spectroscopy (supplementary material,

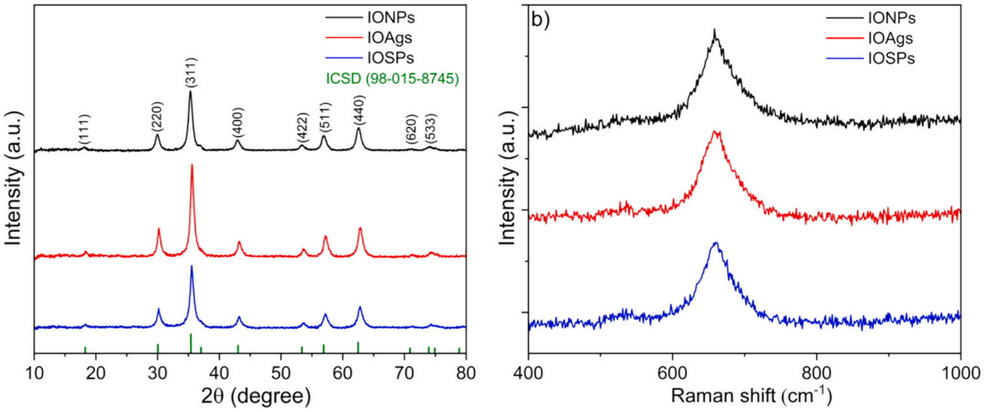

**Fig. 1.** a) XRD patterns and b) Raman spectra for IONPs (black line), IOAgs (red line), and IOSPs powders (blue line). (For interpretation of the references to color in this figure legend, the reader is referred to the web version of this article.)

Fig. S8) indicates the formation of a considerable maghemite phase.

The particle size and morphology of IONPs, IOAgs, and IOSPs samples were studied using SEM and TEM (Fig. 2). IONPs show a spherical-like shape with an average primary particle size of 8.6 nm (supplementary material, Fig. S3a), which matches well with the crystallite size obtained from Rietveld refinement. Besides, magnetic nanoparticles are prone to cluster together as a result of van der Waals forces, as shown in Fig. 2a (right).

For the IOAgs (without PAA) sample, the TEM and SEM images reveal the coexistence of many irregular shaped, buckled agglomerates (highlighted in Fig. 2b, right) and spherical agglomerates with different particle sizes, i.e., pronounced dispersity. This is explained by the collapse of the outer crust formed during droplet evaporation in the spray drying process. In the absence of PAA, this crust lacks strength due to inhomogeneous dispersion of IONPs, leading to irregular agglomerate shapes. The collapse occurs due to the inability of the crust to withstand internal solvent evaporation pressure, highlighting the importance of the crust strength on the final particle morphology [25]. Consistent with the crystallite sizes derived from the diffraction patterns, high magnification TEM (supplementary material, Fig. S3b) also revealed that the average primary particle size increased during the spray drying process without PAA.

When adding PAA to the spray drying feed dispersion, spherical supraparticles are observed (Fig. 2c). We attribute the formation of these porous but still comparatively dense structures to the fact that the introduction of PAA into the IONPs suspension modifies the $\zeta$-potential of the nanoparticles in such a way that homogeneously dispersed nanoparticles exist inside the droplet without the occurrence of sharp

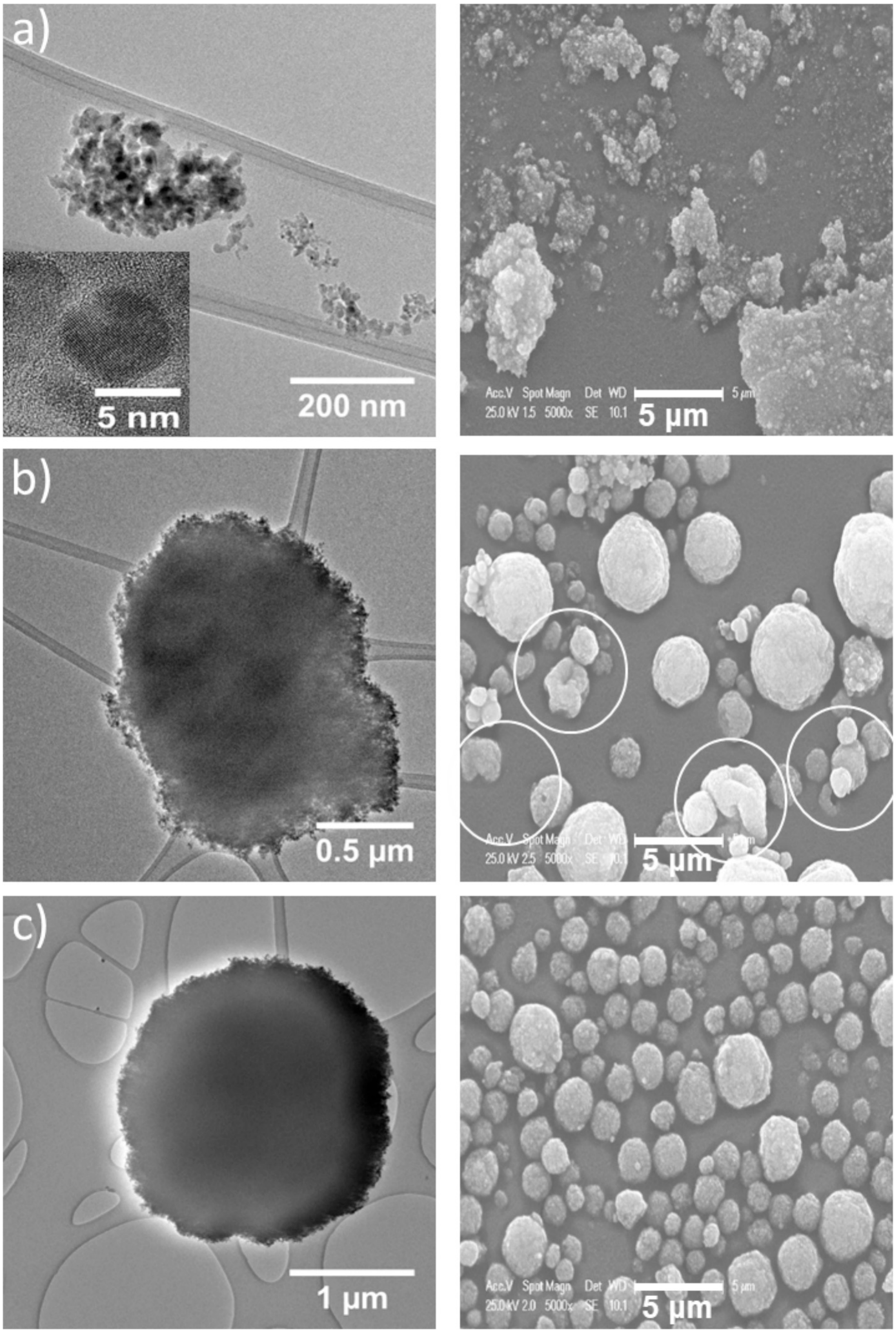

**Fig. 2.** TEM (left) and SEM (right) images of a) IONPs, b) IOAgs, and c) IOSPs dispersed in water.

concentration gradients. In this scenario, smoother and more spherical supraparticles form because of uniform drying rates across the entire droplet surface. Moreover, PAA enhances the early-stage mechanical strength of the crust, thereby preventing later-stage buckling [26].

The specific surface area of the annealed IONPs, IOAgs, and IOSPs powders was determined by $N_2$ sorption analyzed according to BET [27] and resulted in values of 130, 82, and 100 $m^2/g$ for IONPs, IOAgs, and IOSPs samples, respectively. The surface reduction can be explained by the formation of agglomerates during the spray drying process inevitably causing a decrease in the $N_2$-accessible surface area. In case of IOAgs, the low surface area supports the findings of the XRD measurements and electron microscopy that slight particle growth occurred during spray drying. Besides, the porosity of IOAgs and IOSPs was confirmed by MIP (supplementary material, Fig. S4). The isotherm of all the samples showed a typical IV class according to the IU classification of adsorption isotherms [28], demonstrating the presence of mesoporous channels in IOAgs and IOSPs samples, which are favorable for the adsorption of pollutants. Moreover, the pore-size analysis of IOAgs and IOSPs samples by MIP revealed a broad pore size distribution with an average volume accounting to pore sizes of 40 and 22 nm, respectively (supplementary material, Fig. S4). While both IOSPs and IOAgs display broad pore size distributions, IOAgs exhibit a multimodal pore size distribution compared to the unimodal distribution observed in IOSPs. This finding supports the results gained from TEM and SEM images that showed the coexistence of many irregularly shaped agglomerates in IOAgs samples.

### 3.2. Characterization of powders after dispersion in the liquid phase

To estimate the hydrodynamic size ($x_{\mathrm{hyd}}$) of IONPs, IOAgs, and IOSPs after dispersing them in water (5 min bath sonication), respective dispersions were prepared and investigated by dynamic light scattering (DLS). As is shown in Fig. 3a, the average $x_{\mathrm{hyd}}$ of IOAgs and IOSPs particles is obviously higher than that of the IONPs. Moreover, the IOAgs sample exhibits a very broad, at least bimodal particle size distribution, revealing that the sample is strongly polydisperse. In contrast, and directly in line with the SEM measurements and indirectly with MIP, IOSPs exhibit a monomodal and comparatively narrow particle size distribution. With regard to structural integrity, i.e., stability of the supraparticles against decay during dispersion, we found that even after a long time of sonication (30 min), there is no obvious change in the hydrodynamic size of IOSPs (supplementary material, Fig. S5a). This confirms the high mechanical stability of IOSPs, which is particularly desired regarding the resistance of IOSPs against mechanical forces that are inevitably present during the water treatment process.

$\zeta$-potential measurements were used to assess the surface charge and isoelectric point of the particles. Fig. 3b shows the $\zeta$-potential of the IONPs, IOAgs, and IOSPs samples. There is no obvious change in the $\zeta$-potential evolution for IONPs and IOAgs samples. However, after introduction of PAA to IONPs, the $\zeta$-potential and thus the total charge of the particles at pH = 7 increased from −22 to −30 mV, indicating a surface modification of the IONPs with the PAA. The findings regarding the functionalization of IONPs with PAA are further supported by TGA (supplementary material, Fig. S6). Compared to the analysis of IONPs TGA curves, the additional weight loss for IOSPs (4 %, 300–600 °C) is attributed to the decarboxylation and decomposition of PAA.

### 3.2.1. Hansen solubility parameters of IONPs and IOSPs

The Hansen solubility parameters (HSPs) – here understood in the context of similarity – of the IONPs and IOSPs were determined to understand the surface behavior upon interaction with ten probe liquids (see supplementary material, Table S1) based on our recent particle size distribution (PSD)-based method [29] and reported according to the Hansen reporting framework [30] (supplementary material, Fig. S7). Similar to the $\zeta$-potential results, the resulting HSP ranges showed that the addition of 10 % PAA leads to a significant increase of the polar interactions, a slight increase of the hydrogen bonding contributions, and negligible change in the disperse interactions of the spray-dried IOSPs in comparison to the annealed IONPs. Noteworthy, the added PAA introduces carboxyl and hydroxyl surface groups which could lead to the increase of the polar and hydrogen bonding interactions. Fig. 4a summarizes the final HSP spheres as material property that were generated by averaging the HSP ranges while Fig. 4c–d show the individual contributions from each interaction parameter in the form of 2D-projections.

### 3.3. Magnetic properties

The magnetic properties of the IONPs, IOAgs, and IOSPs powders were evaluated at room temperature using a vibrating sample magnetometer. Fig. 5 depicts the room temperature (300 K) hysteresis loops of IONPs, IOAgs, and IOSPs powders. The magnetization curve of IONPs displays superparamagnetic properties (no discernible remanence), which can be assigned to limited volume of the small nanoparticles. Moreover, the IOAgs sample exhibits the same superparamagnetic behavior as IONPs, indicating that the spray drying process did not affect the general magnetic characteristics of IONPs. However, the measurement of the IOSPs sample showed increased high-field (9 T) magnetization values compared to IONPs and IOAgs samples. The difference in magnetization between the IONPs and IOSPs samples could be assigned to the peculiar mesostructure of the supraparticles, including the enhanced magnetic-dipole coupling that increases with the volume of IOSPs generated during the spray drying process [31]. Furthermore, analysis of $\zeta$-potentials and HSPs confirms the successful surface

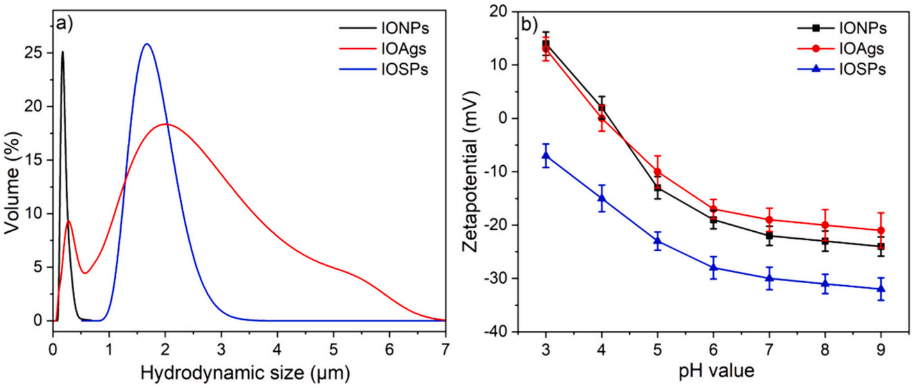

**Fig. 3.** a) Hydrodynamic sizes measured via DLS (Particle size distributions normalized to an area of unity are provided in supplementary material, Fig. S5b and b) $\zeta$-potential measurements of IONPs (black squares), IOAgs (red circles), and IOSPs (blue triangles). (For interpretation of the references to color in this figure legend, the reader is referred to the web version of this article.)

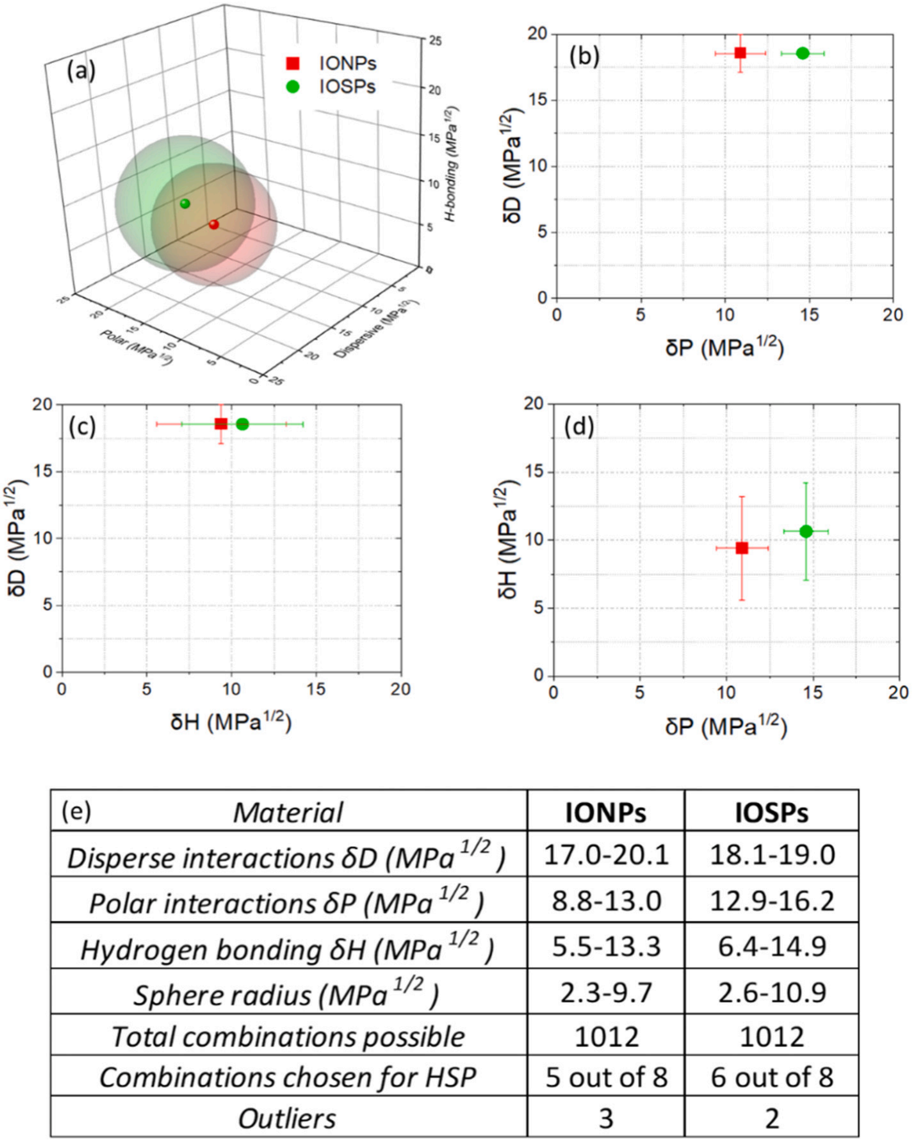

| (e) Material | IONPs | IOSPs |
|---|---|---|
| Disperse interactions δD (MPa $^{1/2}$) | 17.0-20.1 | 18.1-19.0 |
| Polar interactions δP (MPa $^{1/2}$) | 8.8-13.0 | 12.9-16.2 |
| Hydrogen bonding δH (MPa $^{1/2}$) | 5.5-13.3 | 6.4-14.9 |
| Sphere radius (MPa $^{1/2}$) | 2.3-9.7 | 2.6-10.9 |
| Total combinations possible | 1012 | 1012 |
| Combinations chosen for HSP | 5 out of 8 | 6 out of 8 |
| Outliers | 3 | 2 |

**Fig. 4.** Hansen spheres (a) and individual HSPs (b–d) of the IONPs and IOSPs. Table (e) summarizes the final HSP ranges.

modification of IOSPs with PAA, leading to reduced surface spin disorder and enhanced high-field magnetization [32]. Despite this improvement, all samples exhibit a slight increase in magnetization at high fields, typically associated with (surface/interface) spin canting behavior. Mössbauer spectra at 7 T (supplemental material, Fig. S8) indicate a reduced average spin canting angle for IOSPs compared to IONPs, providing evidence of enhanced magnetization upon surface modification. Overall, the samples exhibit superparamagnetic behavior at room temperature, which is important in separation applications where ferromagnetic or ferrimagnetic characteristics should be avoided.

### *3.4. Adsorption performance*

Because of its high saturation magnetization (72 Am$^2$/kg), abundant surface oxygen-containing functional groups (Fig. S2), and its large specific surface area (100 m$^2$/g), IOSPs were chosen for further adsorption testing. The adsorption capacity was investigated on the basis of the uptake rate of pollutants from aqueous media. A concentration of 0.5 g/l IOSPs was selected for the following adsorption experiments. Details are given in the supplementary material, Fig. S9.

#### *3.4.1. pH dependence of the adsorption*

Changing the pH of the medium will affect the charge of both the dissolved metal ions and the adsorbent surface in water. Thus, the influence of pH on the Pb(II) adsorption onto the surface of IONPs and IOSPs was evaluated in the pH range from 3 to 8. As shown in Fig. 6a, the Pb(II) removal efficiency increased significantly as the pH value was raised from 3 to 6, and then the adsorption capacity for Pb(II) remained unchanged when the initial pH was increased to 8. This phenomenon can be explained by considering two aspects:

(i) At low initial pH, an excess of H$^+$ ions competes with the Pb(II) cations for the same active sites on the iron-oxide surface, resulting in a lower adsorption capacity of IOSPs [33], while the removal of Pb(II) by IONPs is almost negligible below pH 5. As shown previously in Fig. 3b, the $\zeta$-potential value of IONPs is positive at low pH and reaches the isoelectric point around pH 4, indicating poor electrostatic attraction between the positively charged Pb(II) and the IONPs surface. The low adsorption efficiency of IONPs is attributed to the ion exchange of Pb(II) with Fe$^{2+}$ ions in the lattice structure of IONPs [34].

(ii) With pH values between 5 and 8, the presence of oxygen-functional groups leads to a more negative surface of both

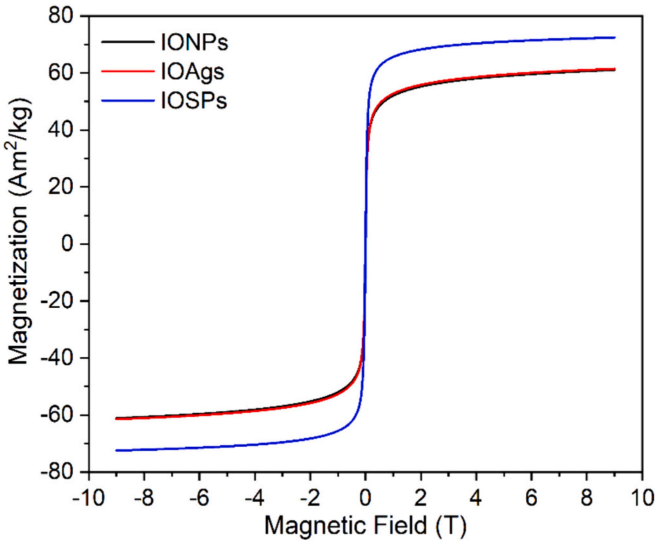

**Fig. 5.** Magnetization curves of IONPs (black), IOAgs (red), and IOSPs (blue) powders recorded at room temperature (300 K). (For interpretation of the references to color in this figure legend, the reader is referred to the web version of this article.)

IONPs and IOSPs (Fig. 3b) which induces a highly desirable electrostatic attraction between particles and Pb(II) ions.

### 3.4.2. Adsorption kinetics for the removal of Pb(II)

The removal efficiency of IONPs and IOSPs for highly concentrated Pb(II) solution (50 mg/l) were analyzed according to the contact time (0–140 min) as shown in Fig. 6b. In the case of IONPs, the Pb(II) adsorption efficiency achieved values close to 15 % within 60 min while the removal efficiency of Pb(II) by IOSPs reached close to 100 % within 60 min. The Pb(II) uptake efficiency by IOSPs adsorbent increased rapidly within the initial 30 min. Subsequently, after 60 min adsorption equilibrium was reached. We attribute the improvement of the adsorption capacity of IOSPs to the following features:

(i) The negative and higher surface charge of the IOSPs boosts the electrostatic attraction between the IOSPs and the metal ions, enabling a faster uptake rate of Pb(II).
(ii) The still large specific surface area in combination with the high pore volume of the IOSPs provides abundant active sites and therefore improves the adsorption capacity of the IOSPs material (as explained later, Fig. 7).
(iii) The presence of PAA that possesses diverse binding sites such as COOH, O—H, and Fe—O on the surfaces of IOSPs enables complexation with metals (as discussed later, Fig. 9) [35].

Moreover, based on the time–dependent sorption data, the kinetic models of pseudo-first order (PFO), pseudo-second order (PSO), and Weber Morris intraparticle diffusion (pore diffusion, WMD) were adjusted using the following equations:

$$q_t = q_e(1 - exp(-k_1\, t)) \tag{3}$$

$$q_t = \frac{k_2\, q_e^2\, t}{1 + k_2\, q_e\, t} \tag{4}$$

$$q_t = k_d\, t^{0.5} + C\, t \tag{5}$$

where $q_t$ (mg/g) is the adsorption capacity at time $t$, $q_e$ is the adsorption capacity at equilibrium, $k_1$, $k_2$, and $k_d$ are the rate constants for PFO, PSO, and WMD, and $C$ is the thickness of the boundary layer.

For IOSPs, the coefficients of determination (0.823 for PFO and 0.930 for PSO) and the close agreement between the theoretical and experimental $q_e$ values initially suggested a good fit of the experimental data to the PSO model (supplementary material, Fig. S10 and Table S2), while the adsorption process of Pb(II) on the IONPs surface can be well

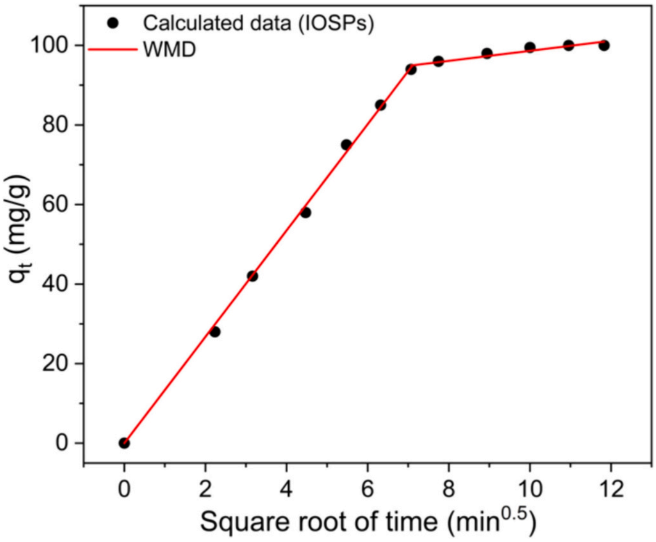

**Fig. 7.** Intraparticle diffusion model for the adsorption of Pb(II) onto IOSPs. Reaction conditions: Pb(II): 50 mg/l; Adsorbent: 0.5 g/l.

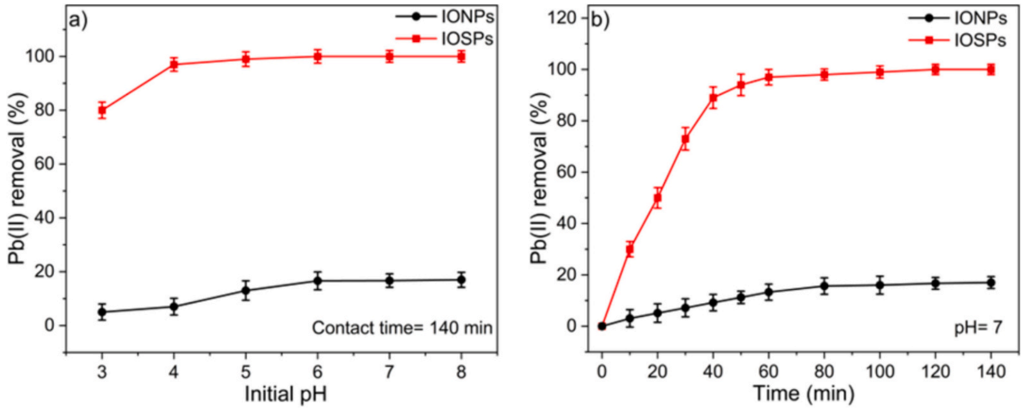

**Fig. 6.** a) Effect of initial pH on the adsorption capacities of Pb(II) by IONPs and IOSPs, and b) removal efficiency of Pb(II) by IONPs and IOSPs. Reaction conditions: Pb(II): 50 mg/l; adsorbent: 0.5 g/l.

described by the PFO model. However, fitting of the PSO model for IOSPs did not reach satisfactory results, therefore the adsorption process might be governed by physical and chemical adsorption. Since both PFO and PSO models cannot describe the mechanism of adsorption, the adsorption kinetics data for IOSPs was further analyzed by the WMD model. The adsorption rate can be expressed by intraparticle diffusion when a linear plot passes close to the origin [36]. As shown in Fig. 7, the adsorption process might occur in two major stages. The first stage is bulk diffusion of Pb(II) ions on the surface of IOSPs, which is the fastest adsorption period. The second is intraparticle or pore diffusion that is a gradual adsorption resulting from the diffusion of Pb(II) through the pores of IOSPs. In addition, no line is close to the origin, suggesting that the adsorption rate might be limited by multiple steps with the contribution of other possible mechanisms such as complexation and physical adsorption.

### *3.4.3. Adsorption isotherms*

To understand the adsorption behavior of IONPs and IOSPs for Pb(II) ions, Langmuir, Freundlich, and Sips adsorption models were employed to simulate the interaction between particles and metal ions and to determine the maximum adsorption capacity ($q_{max}$) of the sample with the initial concentration of the Pb(II) solution ranging from 10 to 500 mg/l at 298 K. The Langmuir, Freundlich, and Sips relationships are given as follows:

$$q_e = \frac{q_{max}\, K_L\, C_e}{1 + K_L\, C_e} \tag{6}$$

$$q_e = K_F\, C_e^{1/n} \tag{7}$$

$$q_e = \frac{q_{max}\, K_s\, C_e^{1/n}}{1 + K_s\, C_e^{1/n}} \tag{8}$$

where, $C_e$ is the equilibrium concentration, $q_{max}$ is the maximum adsorption capacity, $K_L$, $K_F$, and $K_s$ are the constants of the Langmuir, Freundlich, and Sips models, respectively, and $1/n$ is the factor of heterogeneity.

The adsorption isotherms of Pb(II) by IONPs and IOSPs using nonlinear fitting are depicted in Fig. 8, and the relevant parameters are summarized in Table 1. For the IONPs sample, the nonlinear fitting results revealed that the Langmuir model showed a better fitting with a higher correlation coefficient value compared to both Freundlich and Sips models, whereas the adsorption behavior of IOSPs follows the Sips isotherm. According to the Langmuir model, the metal adsorption behavior is based on a monolayer coverage on the homogeneous surface of the adsorbent. In contrast, the Sips model describes the sorption on heterogeneous surface sites of the adsorbent. The adsorption capacity of IOSPs increased rapidly at lower concentrations and the uptake efficiency gradually rose when the solution concentration exceeded 100 mg/l for Pb(II). Moreover, $q_{max}$ of IONPs and IOSPs toward Pb(II) could reach 51 and 728 mg/g, respectively, when the adsorption data was fitted to the Langmuir model. However, it has to be noted that the Langmuir model for the IOSPs sample only fits the experimental data well at a low concentration of Pb(II), while the Sips fitting curve always matches well with the experimental data. Thus, the Sips model better represents the metal adsorption of IOSPs, suggesting the adsorption process of IOSPs to be multilayer and heterogeneous. The maximum adsorption capacity of IOSPs was calculated to be 500 mg/g on the basis of the Sips model. With this value, IOSPs are within the top-ranked

**Table 1**
Fitting parameters of Langmuir, Freundlich, and Sips models for the adsorption of Pb(II) onto IONPs and IOSPs: where $K$ and $q$ represent the adsorption rate constant and the amount of adsorbate adsorbed per unit mass of adsorbent at equilibrium, respectively. $R^2$ is the coefficient of determination.

| Model | Parameters | Samples | |
|---|---|---|---|
| | | IONPs | IOSPs |
| Langmuir | $K_L$ (l/mg) | 0.0085 | 0.0045 |
| | $q_{max}$ (mg/g) | 51 | 728 |
| | $R^2$ | 0.997 | 0.976 |
| Freundlich | $K_F$ ((mg/g)(l/mg)1/$n$) | 3.1 | 18.83 |
| | $n$ | 2.3 | 2.1 |
| | $R^2$ | 0.913 | 0.920 |
| Sips | $K_S$ (l/mg) | 0.0041 | 0.0007 |
| | $q_{max}$ | 46.2 | 500 |
| | $n$ | 0.44 | 1.8 |
| | $R^2$ | 0.993 | 0.999 |

**Table 2**
Comparison of the adsorption capacity of IOSPs toward Pb(II) with recently reported adsorbents.

| Adsorbents | pH | $q_{max}$ (mg/g) | Reference |
|---|---|---|---|
| Hydroxyapatite embedded ferroferric oxide | 4.5 | 1249 | [37] |
| IOSPs | 5 | 500 | This work |
| Ionic liquid functionalized graphene | 5.1 | 406.6 | [38] |
| 3D N-doped carbon-FeMg LDH | 6 | 344.8 | [39] |
| $Fe_3O_4@SiO_2$–mPD/SP | 5 | 190.75 | [40] |
| $Fe_3O_4@SiO_2$-NH-MFL | 5.5 | 150.33 | [41] |
| $Fe_3O_4$/GO/MgAl LDH | 5 | 173.0 | [42] |
| $Fe_3O_4$ polyethyleneimine lignin | 6 | 96.66 | [43] |
| Activated carbon | 6 | 119.32 | [44] |
| Carbon nanotubes/$CoFe_2O_4$ | 6 | 140.1 | [45] |
| Lignin-based $Fe_3O_4$ adsorbents | 5 | 111.23 | [46] |
| Amidoxime-modified mesoporous $SiO_2$ | 4.35 | 83.23 | [47] |

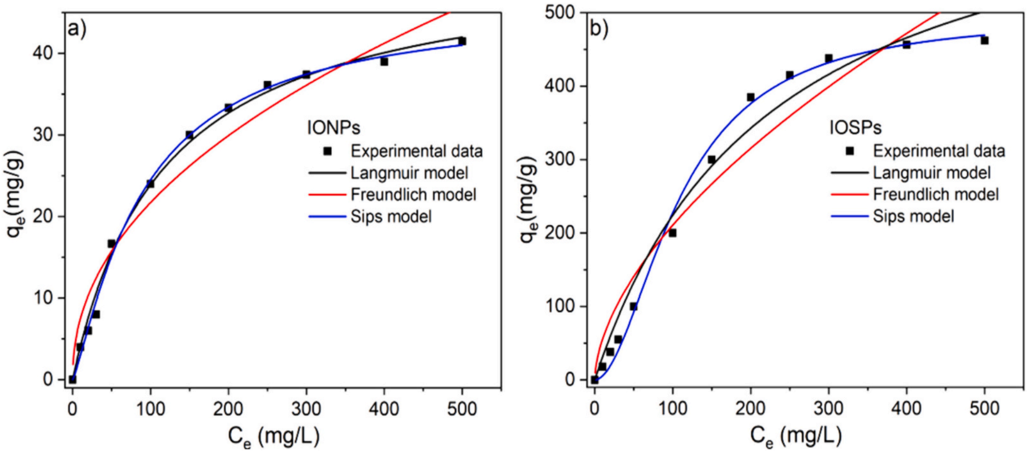

**Fig. 8.** Adsorption isotherm for Pb(II) onto IONPs and IOSPs.

adsorbents among previously reported adsorbents (Table 2). Moreover, our system showed a high resistance to co-existing ions and NOM (Fig. 10 a), proving that the structuring into IOSPs holds promise in real wastewater treatment systems.

### 3.4.4. Adsorption mechanism

To understand the adsorption mechanism of IOSPs, XPS and FTIR spectra before and after the adsorption process were investigated. From fitting the C1s spectra depicted in Fig. 9a, it can be deduced that the proportions of C—C, C—O, and C═O for the fresh IOSPs were determined to be 62, 15, and 23 %, respectively, while after the adsorption process they changed to 61, 6, and 33 %. This indicates that the C—O and C═O groups might play an important role in the adsorption of metals from IOSPs. Moreover, the Fe2p XPS spectrum of the IOSPs sample (Fig. 9b) fitted by peaks at the binding energies of 709.1 and 711.2 eV, are related to Fe$^{2+}$ and Fe$^{3+}$ (Fe2p$_{3/2}$), respectively, whereas the peaks at the binding energies of 722.4 and 724.6 eV are assigned to Fe$^{2+}$ and Fe$^{3+}$ (Fe2p$_{1/2}$) [48]. Furthermore, two satellite peaks located around 717 and 730 eV are typical characteristics of Fe$^{2+}$ in the Fe$_3$O$_4$ structure [49]. However, after the adsorption process, both Fe2p$_{3/2}$ and Fe2p$_{1/2}$ peaks were slightly shifted, which can be ascribed to the formation of strong interactions between Pb(II) and IOSPs during the adsorption process [50]. From the O1s spectra (Fig. 9c) it is seen that the percentage of surface OH increased from 34 to 43 % after the adsorption process revealing chelation or complexation interactions between the surface oxygen functional groups and Pb(II) ions [46]. Besides, FTIR analysis was performed before and after the adsorption process as shown in Fig. 9d. After the adsorption process, the intensity of characteristic peaks of COO$^-$ and OH groups increased along with a slight displacement in their frequency values, demonstrating surface complexation with metal ions [51]. Moreover, the peak around 1700 cm$^{-1}$ mostly vanished after the adsorption process, indicating bidentate chelation of the carboxyl moieties to the metal ion [52]. To summarize, based on both XPS and FTIR results, the possible adsorption interaction of metals with the active sites on IOSPs mainly involves physical adsorption followed by intra-particle diffusion to the interior part and chelation or complexation interactions with the surface oxygen functional groups of IOSPs.

At this point, it needs to be noted that the adsorption mechanism can vary depending on the specific pollutant. While the discussed mechanism may apply to Pb(II), different pollutants may interact differently with the surface of the adsorbent material. Further investigation is needed to determine the specific mechanisms for each pollutant.

### 3.4.5. Effect of NOM and reusability of IOSPs

NOM is a ubiquitous constituent of all natural waters and soils. It is known to be able to block the sorption sites on the adsorbent surface [53], leading to a decrease in the adsorption capacity of the adsorbent. Therefore, the influence of NOM on the Pb(II) removal efficiency was investigated. As shown in Fig. 10a, no significant inhibition regarding the Pb(II) removal was observed with the addition of 10 mg/l NOM as compared to a reference without any NOM. However, increasing the NOM loading to 25 mg/l resulted in a slight decrease in the removal efficiency of Pb(II) by 9 % compared to experiments performed in the absence of NOM. This decrease might be attributed to the chelating interaction of NOM and Pb(II) [54].

Moreover, to evaluate the reusability of the IOSPs, five adsorption-desorption cycles were conducted under identical conditions (Fig. 10b). The used IOSPs were rapidly recovered using a magnet as indicated by the magnetic separation tests (Fig. 10c) and regenerated by placing them in a 0.1 mol/l HCl solution. Interestingly, the reused IOSPs maintained a high adsorption capacity after five adsorption–desorption runs. The slight decrease in the sorption capacity of the IOSPs is due to the mass loss (6 %) of IOSPs during the washing process. This manifests that the IOSPs exhibit excellent stability and regeneration properties through multiple adsorption–desorption cycles. Additionally, we have not studied the effect of the regeneration time on the adsorption performance of the IOSPs adsorbent. Hence, the extend of shortcomings due

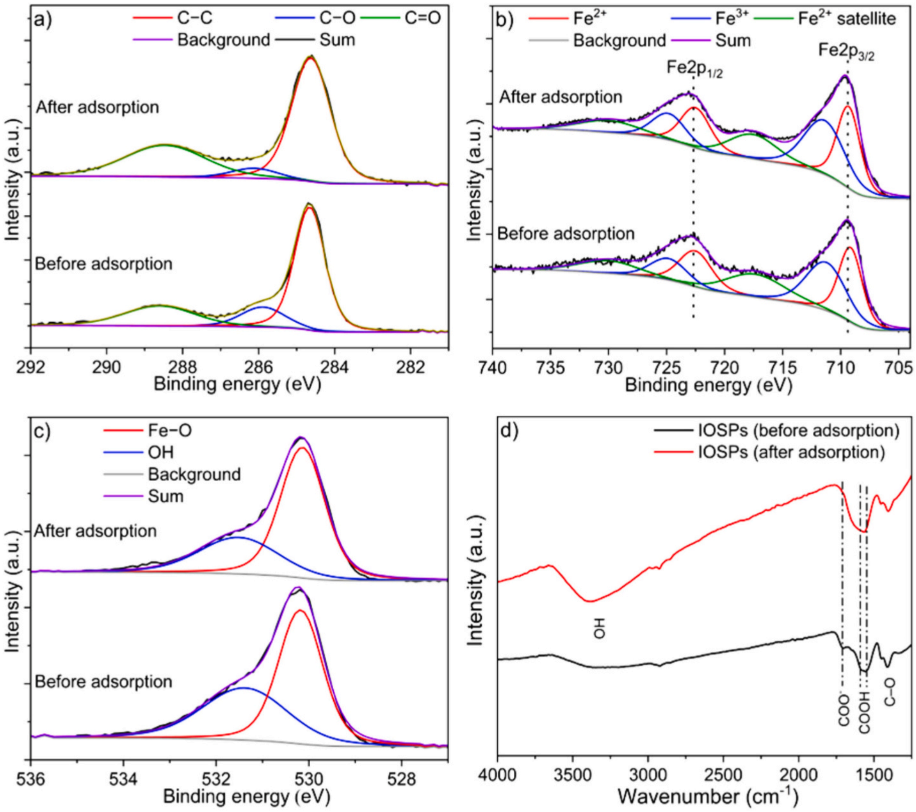

**Fig. 9.** a) C1s, (b) Fe2p, c) O1s, and d) FTIR spectra of IOSPs before and after Pb(II) adsorption.

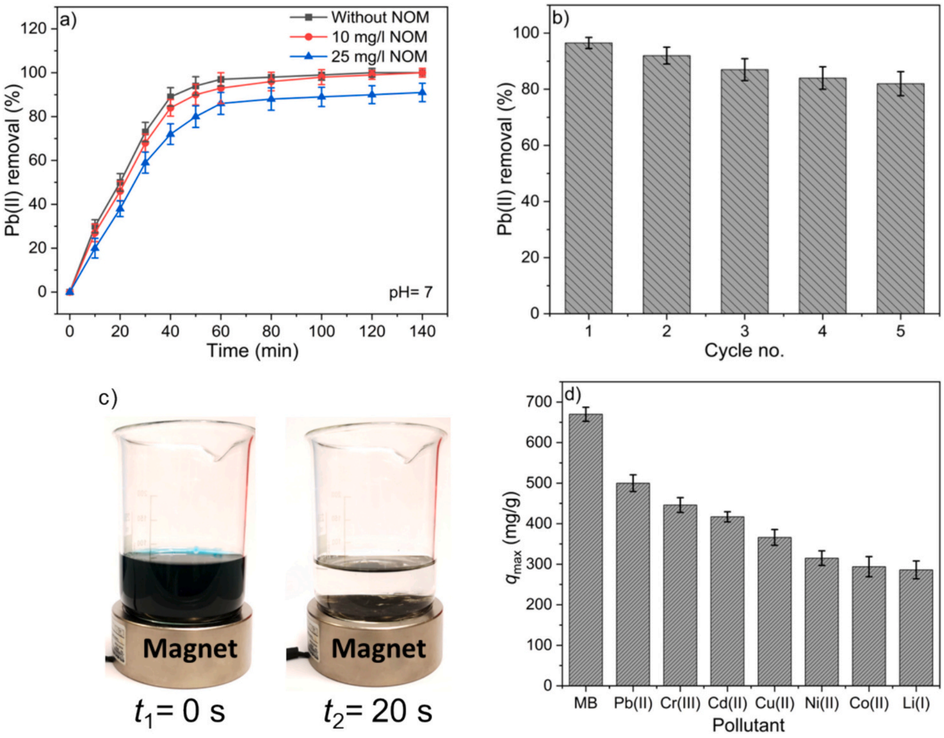

**Fig. 10.** a) Effects of NOM on the Pb(II) removal by IOSPs, b) stability tests of IOSPs through adsorption–desorption cycles, c) photographs of IOSPs aqueous dispersion before and after magnetic separation for 20 s, and d) adsorption performance of IOSPs during the removal of various pollutants.

to prolonged regeneration time needs to be determined in future work. Moreover, we have studied the XRD patterns of fresh and used adsorbent (supplementary material, Fig. S11). The pattern of the repeatedly used adsorbent shows there is no change in the $Fe_3O_4$ phase after the adsorption experiments. However, upon storage at ambient air for several weeks, Mössbauer spectroscopy (supplementary material, Fig. S8) reveals the emergence of a substantial maghemite phase.

### 3.4.6. *Comparison of adsorption capacity of IOSPs with other metal ions*

The adsorption efficiency of the IOSPs has been tested for different kinds of pollutants, which is important for practical water treatment applications. Hence, the adsorption capacities of the IOSPs material for Cr(III), Cd(II), Cu(II), Ni(II), and Co(II) were tested and evaluated individually (Fig. 10d). In addition to the heavy metal ions, the adsorption capacities for Li(I) and the cationic dye MB were analyzed due to their increasing presence and potential environmental impact. IOSPs exhibited the highest adsorption capacities in the trend of Pb(II) or MB > Cr(III) > Cd(II) > Cu(II) > Ni(II) > Co(II) > Li(I). This removal trend can be explained by the Pearson theory of hard and soft acids and bases (HSAB). Based on this theory, the oxygen functional group ligands act as soft bases on the surface of IOSPs, revealing a better affinity for the softest acid metal Pb(II) over other metals [46]. Therefore, IOSPs exhibited an excellent adsorption capacity toward Pb(II) ions. Moreover, the maximum adsorption capacity of IOSPs for MB, Pb(II), Cr(III), Cd(II), Cu(II), Ni(II), Co(II), and Li(I) were calculated to be 670, 500, 446, 417, 366, 315, 294, and 286 mg/g on the basis of the Sips model (supplementary material, Fig. S12). These results indicate that the generated IOSPs represent an outstanding material and potential adsorbent for purifying water bodies from toxic pollutants.

## 4. Conclusions

In this paper, we have demonstrated a scalable and robust method to prepare mechanically stable IOSPs that were used for the removal of toxic pollutants from water. The excellent adsorption capacity of the IOSPs is based on the following six features: Firstly, the high total charge of the IOSPs boosts the electrostatic attraction between the IOSPs and cationic pollutants, leading to an enhanced uptake of pollutant from water bodies. Secondly, the porous structure of IOSPs provides a large surface area that facilitates and improves the accessibility of active sites and therefore exhibits an enhanced removal of pollutant from an aqueous medium. Thirdly, the formation of oxygen functional groups such as COOH, OH, and Fe—O on the surfaces of IOSPs plays an important role in the complexation with pollutants. Fourthly, IOSPs reveal high stability and regeneration performance through multiple adsorption-desorption processes. Fifthly, IOSPs exhibit superparamagnetic behavior despite their multicore structure and can be easily magnetically separated from the treated water due to their high saturation magnetization (ca. 70 $Am^2/kg$). Finally, the IOSPs show an excellent uptake efficiency of different metals and dyes such as Cr(III), Cd(II), Cu(II), Ni(II), Co(II), Li(I), and methylene blue. Hence, the generated IOSPs could be employed as a potential and low-cost adsorbent for the removal of toxic pollutants in the water purification system.

## CRediT authorship contribution statement

**Mohaned Hammad:** Writing – original draft, Validation, Methodology, Investigation, Data curation. **Adil Amin:** Writing – original draft, Validation, Investigation. **Anam Asghar:** Writing – review & editing, Investigation. **Osama Anwar:** Writing – original draft, Investigation. **Soma Salamon:** Writing – review & editing, Writing – original draft, Investigation. **Joachim Landers:** Writing – review & editing, Writing – original draft, Investigation. **Mena-Alexander Kräenbring:** Writing – review & editing, Writing – original draft, Investigation. **Adarsh Jain:** Writing – review & editing, Writing – original draft, Investigation. **Sebastian Hardt:** Writing – review & editing, Writing – original draft, Investigation. **Hartmut Wiggers:** Writing – review & editing, Validation. **Torsten C. Schmidt:** Writing – review & editing, Validation. **Heiko Wende:** Writing – review & editing, Validation. **Christof Schulz:** Writing – review & editing, Validation. **Doris Segets:** Writing – review

& editing, Validation, Supervision, Funding acquisition.

## Declaration of competing interest

The authors declare that they have no known competing financial interests or personal relationships that could have appeared to influence the work reported in this paper.

## Data availability

The data that support the findings of this study is openly available in Zenodo at https://doi.org/10.5281/zenodo.13348534.

## Acknowledgements

This material is based upon work supported by the Mercator Research Center Ruhr (MERCUR) within the DIMENSION project. Financial support by the German Research Foundation (DFG) via the CRC/TRR 247 (Project-ID 388390466) is gratefully acknowledged.

## Appendix A. Supplementary data

Supplementary data to this article can be found online at https://doi.org/10.1016/j.jwpe.2024.106025.

## References

[1] A. Reyes-Calderón, S. Pérez-Uribe, A.G. Ramos-Delgado, S. Ramalingam, G. Oza, R. Parra-Saldívar, R.A. Ramirez-Mendoza, H.M.N. Iqbal, A. Sharma, Analytical and regulatory considerations to mitigate highly hazardous toxins from environmental matrices, J. Hazard. Mater. 423 (2022) 127031, https://doi.org/10.1016/j.jhazmat.2021.127031.

[2] M.A. Mudassir, S.Z. Hussain, A. Jilani, H. Zhang, T.M. Ansari, I. Hussain, Magnetic hierarchically macroporous emulsion-templated poly(acrylic acid)–iron oxide nanocomposite beads for water remediation, Langmuir 35 (2019) 8996–9003, https://doi.org/10.1021/acs.langmuir.9b01121.

[3] Z. Wang, P. Luo, X. Zha, C. Xu, S. Kang, M. Zhou, D. Nover, Y. Wang, Overview assessment of risk evaluation and treatment technologies for heavy metal pollution of water and soil, J. Clean. Prod. 379 (2022) 134043, https://doi.org/10.1016/j.jclepro.2022.134043.

[4] L. Järup, Hazards of heavy metal contamination, Br. Med. Bull. 68 (2003) 167–182, https://doi.org/10.1093/bmb/ldg032.

[5] M. Hammad, P. Fortugno, S. Hardt, C. Kim, S. Salamon, T.C. Schmidt, H. Wende, C. Schulz, H. Wiggers, Large-scale synthesis of iron oxide/graphene hybrid materials as highly efficient photo-Fenton catalyst for water remediation, Environ. Technol. Innov. 21 (2021) 101239, https://doi.org/10.1016/j.eti.2020.101239.

[6] S. Kamari, A. Shahbazi, High–performance nanofiltration membrane blended by Fe3O4@SiO2–CS bionanocomposite for efficient simultaneous rejection of salts/heavy metals ions/dyes with high permeability, retention increase and fouling decline, Chem. Eng. J. 417 (2021) 127930, https://doi.org/10.1016/j.cej.2020.127930.

[7] Y. Li, X. Qi, G. Li, H. Wang, Double-pathway arsenic removal and immobilization from high arsenic-bearing wastewater by using nature pyrite as in situ Fe and S donator, Chem. Eng. J. 410 (2021) 128303, https://doi.org/10.1016/j.cej.2020.128303.

[8] M.R. Awual, Efficient phosphate removal from water for controlling eutrophication using novel composite adsorbent, J. Clean. Prod. 228 (2019) 1311–1319, https://doi.org/10.1016/j.jclepro.2019.04.325.

[9] S. Liu, X. He, Y. Wang, L. Wang, Cleaner and effective extraction and separation of iron from vanadium slag by carbothermic reduction-chlorination-molten salt electrolysis, J. Clean. Prod. 284 (2021) 124674, https://doi.org/10.1016/j.jclepro.2020.124674.

[10] M.B. Poudel, G.P. Awasthi, H.J. Kim, Novel insight into the adsorption of Cr(VI) and Pb(II) ions by MOF derived Co-Al layered double hydroxide @hematite nanorods on 3D porous carbon nanofiber network, Chem. Eng. J. 417 (2021) 129312, https://doi.org/10.1016/j.cej.2021.129312.

[11] S. Cheng, Y. Liu, B. Xing, X. Qin, C. Zhang, H. Xia, Lead and cadmium clean removal from wastewater by sustainable biochar derived from poplar saw dust, J. Clean. Prod. 314 (2021) 128074, https://doi.org/10.1016/j.jclepro.2021.128074.

[12] M. Shi, X. Min, Y. Ke, Z. Lin, Z. Yang, S. Wang, N. Peng, X. Yan, S. Luo, J. Wu, Y. Wei, Recent progress in understanding the mechanism of heavy metals retention by iron (oxyhydr)oxides, Sci. Total Environ. 752 (2021) 141930, https://doi.org/10.1016/j.scitotenv.2020.141930.

[13] X. Zhang, C.M. Navarathna, W. Leng, T. Karunaratne, R.V.K.G. Thirumalai, Y. Kim, C.U. Pittman, T. Mlsna, Z. Cai, J. Zhang, Lignin-based few-layered graphene-encapsulated iron nanoparticles for water remediation, Chem. Eng. J. 417 (2021) 129199, https://doi.org/10.1016/j.cej.2021.129199.

[14] N. Torasso, A. Vergara-Rubio, P. Rivas-Rojas, C. Huck-Iriart, A. Larrañaga, A. Fernández-Cirelli, S. Cerveny, S. Goyanes, Enhancing arsenic adsorption via excellent dispersion of iron oxide nanoparticles inside poly(vinyl alcohol) nanofibers, J. Environ. Chem. Eng. 9 (2021) 104664, https://doi.org/10.1016/j.jece.2020.104664.

[15] K.C. Das, S.S. Dhar, D.G. Thakurata, J. Das, Sn(II) inserted on hyd1. Das KC, Dhar SS, Thakurata DG, Das J. Sn(II) inserted on hydroxyapatite encapsulated nickel ferrite (NiFe2O4@HAp-Sn2+): a novel nanocomposite for the effective photo-degradation of rhodamine B dye, J. Clean. Prod. 290 (2021) 125172, https://doi.org/10.1016/j.jclepro.2020.125172.

[16] K. Mandel, A. Drenkova-Tuhtan, F. Hutter, C. Gellermann, H. Steinmetz, G. Sextl, Layered double hydroxide ion exchangers on superparamagnetic microparticles for recovery of phosphate from waste water, J. Mater. Chem. A 1 (2013) 1840–1848, https://doi.org/10.1039/C2TA00571A.

[17] L. Su, D. Han, G. Zhu, H. Xu, W. Luo, L. Wang, W. Jiang, A. Dong, J. Yang, Tailoring the assembly of iron nanoparticles in carbon microspheres toward high-performance electrocatalytic denitrification, Nano Lett. 19 (2019) 5423–5430, https://doi.org/10.1021/acs.nanolett.9b01925.

[18] L. Kleinfeldt, J. Gädke, R. Biedendieck, R. Krull, G. Garnweitner, Spray-dried hierarchical aggregates of iron oxide nanoparticles and their functionalization for downstream processing in biotechnology, ACS Omega 4 (2019) 16300–16308, https://doi.org/10.1021/acsomega.9b01549.

[19] S. Mondini, M. Leonzino, C. Drago, A.M. Ferretti, S. Usseglio, D. Maggioni, P. Tornese, B. Chini, A. Ponti, Zwitterion-coated iron oxide nanoparticles: surface chemistry and intracellular uptake by hepatocarcinoma (HepG2) cells, Langmuir 31 (2015) 7381–7390, https://doi.org/10.1021/acs.langmuir.5b01496.

[20] S. Wintzheimer, T. Granath, M. Oppmann, T. Kister, T. Thai, T. Kraus, N. Vogel, K. Mandel, Supraparticles: functionality from uniform structural motifs, ACS Nano 12 (2018) 5093–5120, https://doi.org/10.1021/acsnano.8b00873.

[21] A. Amin, M. Loewenich, S.O. Kilian, T. Wassmer, S. Bade, J. Lyubina, H. Wiggers, F. Özcan, D. Segets, One-step non-reactive spray drying approach to produce silicon/carbon composite-based hierarchically structured supraparticles for lithium-ion battery anodes, J. Electrochem. Soc. 170 (2023) 20523, https://doi.org/10.1149/1945-7111/acb66b.

[22] M. Hammad, S. Hardt, B. Mues, S. Salamon, J. Landers, I. Slabu, H. Wende, C. Schulz, H. Wiggers, Gas-phase synthesis of iron oxide nanoparticles for improved magnetic hyperthermia performance, J. Alloys Compd. 824 (2020), https://doi.org/10.1016/j.jallcom.2020.153814.

[23] A.V. Anupama, W. Keune, B. Sahoo, Thermally induced phase transformation in multi-phase iron oxide nanoparticles on vacuum annealing, J. Magn. Magn. Mater. 439 (2017) 156–166, https://doi.org/10.1016/j.jmmm.2017.04.094.

[24] S.J. Oh, D.C. Cook, H.E. Townsend, Characterization of iron oxides commonly formed as corrosion products on steel, Hyperfine Interact. 112 (1998) 59–66, https://doi.org/10.1023/A:1011076308501.

[25] E. Lintingre, F. Lequeux, L. Talini, N. Tsapis, Control of particle morphology in the spray drying of colloidal suspensions, Soft Matter 12 (2016) 7435–7444, https://doi.org/10.1039/C6SM01314G.

[26] S. Tanaka, C. Chia-Pin, Z. Kato, K. Uematsu, Effect of internal binder on microstructure in compacts made from granules, J. Eur. Ceram. Soc. 27 (2007) 873–877, https://doi.org/10.1016/j.jeurceramsoc.2006.04.038.

[27] S. Brunauer, P.H. Emmett, E. Teller, Adsorption of gases in multimolecular layers, J. Am. Chem. Soc. 60 (1938) 309–319, https://doi.org/10.1021/ja01269a023.

[28] Porosity of chemically modified silica gels by nitrogen adsorption, positron annihilation and small angle X-ray scattering, in: J. Goworek, A. Borówka, S. Pikus, J. Wawryszczuk, F. Rodriguez-Reinoso, B. McEnaney, J. Rouquerol, K.B.T.-S. in S. S., C. Unger (Eds.), Charact. Porous Solids VI, Elsevier, 2002, pp. 655–662, https://doi.org/10.1016/S0167-2991(02)80193-8.

[29] O. Anwar, S. Bapat, J. Ahmed, X. Xie, J. Sun, D. Segets, Hansen parameter evaluation for the characterization of titania photocatalysts using particle size distributions and combinatorics, Nanoscale 14 (2022) 13593–13607, https://doi.org/10.1039/D2NR02711A.

[30] S. Bapat, S.O. Kilian, H. Wiggers, D. Segets, Towards a framework for evaluating and reporting Hansen solubility parameters: applications to particle dispersions, Nanoscale Adv. 3 (2021) 4400–4410, https://doi.org/10.1039/d1na00405k.

[31] I.S. Smolkova, N.E. Kazantseva, V. Babayan, J. Vilcakova, N. Pizurova, P. Saha, The role of diffusion-controlled growth in the formation of uniform iron oxide nanoparticles with a link to magnetic hyperthermia, Cryst. Growth Des. 17 (2017) 2323–2332, https://doi.org/10.1021/acs.cgd.6b01104.

[32] Y. Yuan, D. Rende, C.L. Altan, S. Bucak, R. Ozisik, D.-A. Borca-Tasciuc, Effect of surface modification on magnetization of iron oxide nanoparticle colloids, Langmuir 28 (2012) 13051–13059, https://doi.org/10.1021/la3022479.

[33] D. Tiwari Lalchhingpuii, S.M. Lee Lalhmunsiama, Chitosan templated synthesis of mesoporous silica and its application in the treatment of aqueous solutions contaminated with cadmium(II) and lead(II), Chem. Eng. J. 328 (2017) 434–444, https://doi.org/10.1016/j.cej.2017.07.053.

[34] I. Uogintė, G. Lujanienė, K. Mažeika, Study of Cu (II), Co (II), Ni (II) and Pb (II) removal from aqueous solutions using magnetic Prussian blue nano-sorbent, J. Hazard. Mater. 369 (2019) 226–235, https://doi.org/10.1016/j.jhazmat.2019.02.039.

[35] J. Xiao, R. Hu, G. Chen, B. Xing, Facile synthesis of multifunctional bone biochar composites decorated with Fe/Mn oxide micro-nanoparticles: physicochemical properties, heavy metals sorption behavior and mechanism, J. Hazard. Mater. 399 (2020) 123067, https://doi.org/10.1016/j.jhazmat.2020.123067.

[36] W.W. J., M.J. Carrell, Kinetics of adsorption on carbon from solution, J. Sanit. Eng. Div. 89 (1963) 31–59, https://doi.org/10.1061/JSEDAI.0000430.

[37] L. Cui, W. Xu, X. Guo, Y. Zhang, Q. Wei, B. Du, Synthesis of strontium hydroxyapatite embedding ferroferric oxide nano-composite and its application in Pb2+ adsorption, J. Mol. Liq. 197 (2014) 40–47, https://doi.org/10.1016/j.molliq.2014.04.027.

[38] X. Deng, L. Lü, H. Li, F. Luo, The adsorption properties of Pb(II) and Cd(II) on functionalized graphene prepared by electrolysis method, J. Hazard. Mater. 183 (2010) 923–930, https://doi.org/10.1016/j.jhazmat.2010.07.117.

[39] L. Ling, W.-J. Liu, S. Zhang, H. Jiang, Achieving high-efficiency and ultrafast removal of Pb(ii) by one-pot incorporation of a N-doped carbon hydrogel into FeMg layered double hydroxides, J. Mater. Chem. A 4 (2016) 10336–10344, https://doi.org/10.1039/C6TA02737G.

[40] E.S. Behbahani, K. Dashtian, M. Ghaedi, Fe3O4-FeMoS4: promise magnetite LDH-based adsorbent for simultaneous removal of Pb (II), Cd (II), and Cu (II) heavy metal ions, J. Hazard. Mater. 410 (2021) 124560, https://doi.org/10.1016/j.jhazmat.2020.124560.

[41] Y. Zhang, S. Ni, X. Wang, W. Zhang, L. Lagerquist, M. Qin, S. Willför, C. Xu, P. Fatehi, Ultrafast adsorption of heavy metal ions onto functionalized lignin-based hybrid magnetic nanoparticles, Chem. Eng. J. 372 (2019) 82–91, https://doi.org/10.1016/j.cej.2019.04.111.

[42] F. Zhang, Y. Song, S. Song, R. Zhang, W. Hou, Synthesis of magnetite–graphene oxide-layered double hydroxide composites and applications for the removal of Pb (II) and 2,4-dichlorophenoxyacetic acid from aqueous solutions, ACS Appl. Mater. Interfaces 7 (2015) 7251–7263, https://doi.org/10.1021/acsami.5b00433.

[43] X. Zhang, Y. Li, Y. Hou, Preparation of magnetic polyethylenimine lignin and its adsorption of Pb(II), Int. J. Biol. Macromol. 141 (2019) 1102–1110, https://doi.org/10.1016/j.ijbiomac.2019.09.061.

[44] M. Kavand, P. Eslami, L. Razeh, The adsorption of cadmium and lead ions from the synthesis wastewater with the activated carbon: optimization of the single and binary systems, J. Water Process Eng. 34 (2020) 101151, https://doi.org/10.1016/j.jwpe.2020.101151.

[45] L. Zhou, L. Ji, P.-C. Ma, Y. Shao, H. Zhang, W. Gao, Y. Li, Development of carbon nanotubes/CoFe2O4 magnetic hybrid material for removal of tetrabromobisphenol A and Pb(II), J. Hazard. Mater. 265 (2014) 104–114, https://doi.org/10.1016/j.jhazmat.2013.11.058.

[46] X. Zhou, C. Jin, G. Liu, G. Wu, S. Huo, Z. Kong, Functionalized lignin-based magnetic adsorbents with tunable structure for the efficient and selective removal of Pb(II) from aqueous solution, Chem. Eng. J. 420 (2021) 130409, https://doi.org/10.1016/j.cej.2021.130409.

[47] L. Tan, J. Xu, X. Xue, Z. Lou, J. Zhu, S.A. Baig, X. Xu, Multifunctional nanocomposite Fe3O4@SiO2–mPD/SP for selective removal of Pb(ii) and Cr(vi) from aqueous solutions, RSC Adv. 4 (2014) 45920–45929, https://doi.org/10.1039/C4RA08040H.

[48] A.P. Grosvenor, B.A. Kobe, M.C. Biesinger, N.S. McIntyre, Investigation of multiplet splitting of Fe 2p XPS spectra and bonding in iron compounds, Surf. Interface Anal. 36 (2004) 1564–1574, https://doi.org/10.1002/sia.1984.

[49] S. Mathur, M. Veith, V. Sivakov, H. Shen, V. Huch, U. Hartmann, H.-B. Gao, Phase-selective deposition and microstructure control in iron oxide films obtained by single-source CVD, Chem. Vap. Depos. 8 (2002) 277–283, https://doi.org/10.1002/1521-3862(20021203)8:6<277::AID-CVDE277>3.0.CO;2-8.

[50] J. Song, Z. Huang, M. Gamal El-Din, Adsorption of metals in oil sands process water by a biochar/iron oxide composite: influence of the composite structure and surface functional groups, Chem. Eng. J. 421 (2021) 129937, https://doi.org/10.1016/j.cej.2021.129937.

[51] R.R. Pawar, Lalhmunsiama, M. Kim, J.-G. Kim, S.-M. Hong, S.Y. Sawant, S.M. Lee, Efficient removal of hazardous lead, cadmium, and arsenic from aqueous environment by iron oxide modified clay-activated carbon composite beads, Appl. Clay Sci. 162 (2018) 339–350, https://doi.org/10.1016/j.clay.2018.06.014.

[52] N. Shukla, C. Liu, P.M. Jones, D. Weller, FTIR study of surfactant bonding to FePt nanoparticles, J. Magn. Magn. Mater. 266 (2003) 178–184, https://doi.org/10.1016/S0304-8853(03)00469-4.

[53] M. Hammad, S. Angel, A.K. Al-kamal, A. Asghar, A. Said Amin, M.-A. Kräenbring, H.T.A. Wiedemann, V. Vinayakumar, M. Yusuf Ali, P. Fortugno, C. Kim, T. C. Schmidt, C.W.M. Kay, C. Schulz, D. Segets, H. Wiggers, Synthesis of novel LaCoO3/graphene catalysts as highly efficient peroxymonosulfate activator for the degradation of organic pollutants, Chem. Eng. J. (2022) 139900, https://doi.org/10.1016/j.cej.2022.139900.

[54] Y. Liu, Z. Lou, Y. Sun, X. Zhou, S.A. Baig, X. Xu, Influence of complexing agent on the removal of Pb(II) from aqueous solutions by modified mesoporous SiO2, Microporous Mesoporous Mater. 246 (2017) 1–13, https://doi.org/10.1016/j.micromeso.2017.03.005.